The Astrophysical Journal, 771:32 (8pp), 2013 July 1 doi:10.1088/0004-637X/771/1/32

COMPARISON OF SOLAR SURFACE FLOWS INFERRED FROM TIME–DISTANCE HELIOSEISMOLOGY AND COHERENT STRUCTURE TRACKING USING HMI/*SDO* OBSERVATIONS

Michal Švanda[1,2], Thierry Roudier[3], Michel Rieutord[3], Raymond Burston[4], and Laurent Gizon[4,5]
[1] Astronomical Institute, Academy of Sciences of the Czech Republic (v. v. i.), Fričova 298, CZ-25165 Ondřejov, Czech Republic; michal@astronomie.cz
[2] Charles University in Prague, Faculty of Mathematics and Physics, V Holešovičkách 2, CZ-18000 Prague 8, Czech Republic
[3] Institut de Recherche en Astrophysique et Planétologie, Université de Toulouse, 14 avenue Edouard Belin, F-31400, Toulouse, France
[4] Max-Planck-Institut für Sonnensystemforschung, Max-Planck-Straße 2, D-37191 Katlenburg-Lindau, Germany
[5] Institut für Astrophysik, Georg-August-Universität Göttingen, D-37077 Göttingen, Germany
Received 2013 March 15; accepted 2013 May 3; published 2013 June 12

ABSTRACT

We compare measurements of horizontal flows on the surface of the Sun using helioseismic time–distance inversions and coherent structure tracking of solar granules. Tracking provides two-dimensional horizontal flows on the solar surface, whereas the time–distance inversions estimate the full three-dimensional velocity flows in the shallow near-surface layers. Both techniques use Helioseismic and Magnetic Imager observations as input. We find good correlations between the various measurements resulting from the two techniques. Further, we find a good agreement between these measurements and the time-averaged Doppler line-of-sight velocity, and also perform sanity checks on the vertical flow that resulted from the three-dimensional time–distance inversion.

Key words: Sun: helioseismology – Sun: interior

Online-only material: color figures

1. MOTIVATION

The Sun is a very dynamic system, where plasma flows play a very important role in solar dynamo processes. The solar dynamo changes the solar magnetic fields and gives rise to all phenomena of solar activity. Thus, the measurement of plasma flows is an important part in understanding the physics of the Sun. Plasma flows in the solar photosphere were studied in the past by many authors using many methods: some methods are straightforward and intuitive, whereas some are more complex. Although there is general agreement on the multiscale structure of these flows, details still differ with the method used to infer these flows. It is not easy to answer which method gives the most accurate results. However, by directly comparing various methods one can gain confidence in the trustworthiness of the results.

1.1. Comparisons between Methods

Not counting the direct measurement of the line-of-sight component of the three-dimensional plasma flow vector, there are two principal methods for measuring velocity fields on the solar surface. The first is based on tracking of the structures (granules, supergranules, magnetic elements, etc.) carried by the underlying flow in the series of frames capturing the same region on the Sun. These provide in general two (horizontal) components of the flow. The second (helioseismology) is based on the analysis of the propagation of solar waves through the convective envelope and can, in principle, provide us with all three components of the flow velocity vector.

Both methods have been carefully tested, usually by utilizing known inputs from numerical simulations (e.g., Rieutord et al. 2001) or by comparing applications of the methods to data from different sources. Švanda et al. (2006) validated and calibrated the local correlation tracking (LCT) method (November 1986) applied to Michelson Doppler Imager (MDI) full-disk Dopplergrams. Recently, Roudier et al. (2013) applied their coherent structure tracking (CST) code to both full-disk Helioseismic and Magnetic Imager (HMI) and *Hinode* intensitygrams. The agreement between the results inferred from completely different sources was great, except for a systematic error in lower-resolution *Solar Dynamics Observatory* (*SDO*)/HMI velocity maps near the solar limb. A correction curve was derived based on this comparison.

Helioseismic methods were validated in a similar manner. Georgobiani et al. (2007) applied time–distance (Duvall et al. 1993) methods to a numerical simulation of near-surface convection, where the solar waves are naturally excited. They used only the surface gravity (f) mode to derive the horizontal surface flow field by means of scaling the travel-time maps (thus no inversion was performed; such an approach is acceptable for the f mode when the surface flow is in question). The comparison of the horizontal (v_x and v_y components) flow maps to the known flows in the simulation ended up with highly positive correlation coefficients (0.70 for v_x and 0.73 for v_y). At the same time, they also applied LCT to the series of simulated intensitygrams with a correlation of 0.99 to the known flows for both components. However, the authors did not mention a direct comparison of time–distance and LCT velocity maps. Zhao et al. (2007) used the same numerical simulation as Georgobiani et al. (2007) to validate a proper time–distance inversion for flows with a correlation of the resulting surface flow maps with the known flows in the simulation of 0.72 for v_x, 0.64 for v_y, and -0.72 for vertical v_z. Note especially the significant anti-correlation in the vertical flow inversion. It was discussed that this is due to the presence of a cross-talk (i.e., leakage of the horizontal components into the vertical one in the mass-conserving flow).

This conclusion was largely confirmed by Švanda et al. (2011), who validated a brand-new time–distance inversion code against synthetic data coming from a numerical simulation of Sun-like convection. Only the inverse modeling part of the whole processing pipeline was validated, which allowed us to avoid possible problems in the travel-time measurements and to study all components of the inversion in detail. It turned out that, indeed, for weak vertical flow inversions the

cross-talk contributions from horizontal components are larger than the proper signal of the vertical flow. The cross-talk component was also highly anti-correlated, which explains the negative sign noted by Zhao et al. (2007). A method of minimization of such cross-talks was invented and successfully implemented. The flow estimates from the inversion compared well to the input flows from the numerical simulation with a correlation coefficient of 0.9 for horizontal components in the near-surface layers and of 0.8 for the vertical component (before the minimization of the cross-talk, it was −0.63).

Recently, similar end-to-end validation of the inversion pipeline for helioseismic holography (including the measurement of helioseismic observables) was performed by Dombroski et al. (2013). The validation was successful in terms of horizontal components and failed (again, due to the cross-talk contributions) for the vertical component.

Comparisons between different methods for retrieving velocity fields have also been done in the past. Hindman et al. (2004) compared the results of two distinct helioseismic methods, ring-diagram and time–distance inversions, with a high correlation (∼0.8) between the different flow estimates. A general conclusion was that the two distinct helioseismic methods observed the same Sun. De Rosa et al. (2000) compared the horizontal divergence of the flow computed from the horizontal velocity maps measured by means of LCT and a proxy for flow divergence from time–distance *f*-mode travel-time maps. The correlation of the two methods was 0.89 when the different resolutions of the horizontal divergence estimates were taken into account. Inconclusive results were obtained by Ambrož (2005), using flow maps derived from a series of low-resolution full-disk magnetograms measured by means of LCT when compared to down-sampled velocity maps from time–distance helioseismology. The correlation coefficient describing the match of the velocity maps that resulted from the two methods was close to zero; however, there were compact and continuous regions of characteristic size from 30 to 60 heliographic degrees with good agreement between the two methods, so that one could not conclude that the results were completely different. Švanda et al. (2007) directly compared surface flow maps obtained using LCT applied to *Solar and Heliospheric Observatory*/MDI full-disk Dopplergrams and using time–distance helioseismology. The map-to-map correlation coefficient was 0.82 for the component of the flow in the direction of solar rotation (which was not removed and thus the correlation was dominated by rotation) and 0.58 for the component in the south–north direction. The effective resolution of the maps compared was set by the size of the LCT apodization window and was around 44 Mm.

To our knowledge, the direct validation of the time–distance inversion pipeline (including the travel-time measurements) and tracking measurements on smaller-than-supergranular scales has not been published. However, it is an important task and must be accomplished when the robustness and trustworthiness of helioseismic flow maps come into question. The aim of this study is to perform end-to-end testing of the time–distance inversion pipeline running at the Max-Planck-Institut für Sonnensystemforschung (MPS) in Katlenburg-Lindau, Germany and also newly implemented at the Astronomical Institute of the Academy of Sciences in Ondřejov, Czech Republic. By testing the measurements of surface flow, we inherently gain more confidence in our knowledge of the flow below the surface and measured by the time–distance helioseismology, which certainly has consequences for the physics of these flows.

2. MEASURED SURFACE FLOWS

We measured surface flow fields using the two distinct methods (tracking and time–distance inversion) applied to data series observed by HMI (Scherrer et al. 2012; Schou et al. 2012) on board the *SDO* satellite on 2010 May 12 and 13. The results were compared to test the correctness of the helioseismic inverse modeling.

2.1. Flow Estimate from Granulation Tracking

One implementation of the tracking methods has the form of CST (Rieutord et al. 2007). The new implementation of the algorithm (Roudier et al. 2012) is split into three main steps:

1. In each frame of the series of intensitygrams, individual granules are segmented out. The segmentation is based on localization of local maxima of intensity, which are tagged as granular centers, through the intensity curvature. The edges or granular cells are detected by extension of regions around the detected centers with points whose minimal curvature value (evaluated in eight directions from the surrounding pixels) is greater than a given threshold, while keeping the minimum distance of one pixel between each pair of granules. In this way, there is control over the size of the segmented structures. Each granule is then identified and tagged.
2. For each granule, the trajectory throughout the data series is drawn by cross-identifying the granules in consecutive frames of data series. Strong assumptions apply in this step. Granules are cross-identified by taking into account a common granule area in the consecutive frames of the series with a threshold that is determined by an upper bound on velocity (measured as displacement divided by time lag between the frames). Typically, velocities larger than 7 km s^{-1} are rejected. The detected trajectories are usually averaged over a time window, and the average velocity is then computed as total displacement change divided by the length of the time window.
3. It is clear that the velocity field derived in the previous step is irregularly spaced. For further analysis, it is necessary to approximate the velocity field by the best differentiable field. This is done using multi-resolution analysis (e.g., Mallat 1989), where the irregular velocity field is expressed in wavelet components with different scales. The differentiable field is then reconstructed from these components.

The CST algorithm has been utilized in many papers (e.g., Tkaczuk et al. 2007; Rieutord et al. 2008, 2010; Roudier et al. 2012, to name a few) and has proven its usefulness in studies of surface velocity fields.

We applied the code to a series of HMI full-disk intensitygrams. The implementation of the CST algorithm used in this study is not sensitive to the signal of oscillations in intensity images, and thus it is not filtered out. The total data series spanned two full days and this was split into shorter series to capture the evolution of surface flows. Each map was computed with a 30 minute time window, and thus we computed 96 maps of the horizontal components of the flow over the two days studied. The results computed using the full resolution of HMI were binned seven times to increase signal-to-noise ratio. The random-error estimate is 250 m s^{-1} for each 30 minute map (Roudier et al. 2012). In these maps, motions within supergranules visually dominate the flow field.

Table 1
Datacubes used in the Comparative Analysis: Temporal Coverage and Carrington Coordinates (l_0 for Longitude and b_0 for Latitude) of the Central Point

Cube No.	Time Range	b_0	l_0	No. Missing Frames
1	2012 May 12 00:01:30–12:01:30 TAI	−3.00	324.94	12
2	2012 May 12 12:01:30–24:01:30 TAI	−3.00	318.33	6
3	2012 May 13 00:01:30–12:01:30 TAI	−3.00	311.72	6
4	2012 May 13 12:01:30–24:01:30 TAI	−3.00	305.11	6

Note. Also number of missing frames (out of 961) are given for a curious reader.

2.2. Flow Estimate from Time–Distance Inversion

The saying "someone's noise is someone else's signal" is especially true for helioseismologists (for a recent review, see Gizon et al. 2010). The time series of observations contains not only the convective motions but also solar oscillations. In the previous method, the signal of solar oscillations did not carry any useful information that could be used by the CST algorithm, and could thus be easily removed without having any effect on the analysis. However, the solar oscillations observed in surface measurements are manifestations of seismic waves traveling through the solar interior, where their propagation is affected by anomalies in plasma state parameters. The deviations in travel times of solar waves can be measured and used in order to dig out the information about these anomalies. Here we focus on the inference of flows, which have the largest impact on *difference* travel times, i.e., the difference between the measured travel times of waves traveling in opposite directions.

Time–distance helioseismology (Duvall et al. 1993) is a set of tools useful for measuring and interpreting wave travel times. It consists of the following steps.

1. Wave travel times are best measured from a series of full-disk maps of line-of-sight velocity (Dopplergrams). HMI provides such measurements with high cadence (45 s) thus providing us with almost ideal data sets. The data sets are tracked and remapped to Postel projection using standard data processing techniques. We track only the disk-center region (512 × 512 pixels) with a constant pixel size of 1.46 Mm for 12 hr. Thus, we obtained four consecutive 12 hr Dopplergram datacubes suitable for travel-time measurements (see Table 1). We focus on a small patch near the disk center, and thus Postel projection approximates the Cartesian coordinate system (x, y, z), where x is in the direction of solar rotation, y in the solar south to north direction, and z indicates height. In the small field of view, the deviations of the Postel-projected coordinates from the Cartesian system are negligible.
2. The datacubes were spatio-temporarily filtered to separate different modes of solar waves. In this study we use only the surface gravity (f) mode.
3. The travel times were measured following the approach of Gizon & Birch (2004). It provides linearized fitting of travel times from measured signal cross-covariances and is robust in the presence of noise. Travel times were measured for center-to-annulus and center-to-quadrant geometries (Duvall et al. 1997) with radii of the annuli 5–20 pixels, thus providing a set of 48 travel-time maps for each of the four Dopplergram datacubes.
4. These travel times are inverted for flows using inversion weights, which are described separately.

2.2.1. Time–Distance Inversion

We assume that there is a linear relationship between the measured travel-time deviations $\delta\tau$ and velocity vector $\boldsymbol{v}$ given by

$$\delta\tau^a(\boldsymbol{r}) = \int_\odot \boldsymbol{K}^a(\boldsymbol{r}' - \boldsymbol{r}, z) \cdot \boldsymbol{v}(\boldsymbol{r}', z)\, \mathrm{d}^2\boldsymbol{r}'\, \mathrm{d}z + n^a(\boldsymbol{r}). \quad (1)$$

Here $\boldsymbol{K}^a = (K^a_x, K^a_y, K^a_z)$ is a vector travel-time sensitivity kernel computed using the Born approximation (Birch & Gizon 2007), $\boldsymbol{r} = (x, y)$ is a horizontal position vector, and the index a uniquely refers to a particular geometry of the travel-time measurement.

We attempt to invert for $\boldsymbol{v}$ from (1) when $\delta\tau$ and $\boldsymbol{K}$ are known. A realization of the random noise n^a is not known; however, its covariance matrix was measured from the data using the $1/T$ fitting approach (for details, see Gizon & Birch 2004), where T is the length of observation. The inversion can be solved by means of a Subtractive Optimally Localized Averaging (SOLA; Pijpers & Thompson 1992) approach. The SOLA technique is standard in time–distance helioseismology (e.g., Jackiewicz et al. 2008). It aims to construct a spatially bound averaging kernel by linearly combining the set of sensitivity kernels while keeping the error magnification under control. The estimate for the flow component v^{inv}_α, where $\alpha = x, y, z$, is then given by

$$v^{\mathrm{inv}}_\alpha(\boldsymbol{r}_0, z_0) = \sum_a \int w^\alpha_a(\boldsymbol{r}' - \boldsymbol{r}_0; z_0)\tau^a(\boldsymbol{r}')\mathrm{d}^2\boldsymbol{r}', \quad (2)$$

where w^α_a are the inversion weights to be determined.

The inverted flow velocity is then a combination of (1) a true velocity component smoothed by the averaging kernel $\mathcal{K}^\alpha_\alpha$, (2) cross-talk from other components, which we attempt to minimize, and (3) a random-noise component $v^{\mathrm{noise}}_\alpha$, the root-mean-square value of which (σ_α) we bound

$$v^{\mathrm{inv}}_\alpha(\boldsymbol{r}_0, z_0) = \int_\odot \mathcal{K}^\alpha_\alpha(\boldsymbol{r} - \boldsymbol{r}_0, z; z_0) v_\alpha(\boldsymbol{r}, z)\mathrm{d}^2\boldsymbol{r}\mathrm{d}z + \sum_{\beta\neq\alpha} \int_\odot \mathcal{K}^\alpha_\beta(\boldsymbol{r} - \boldsymbol{r}_0, z; z_0) v_\beta(\boldsymbol{r}, z)\mathrm{d}^2\boldsymbol{r}\mathrm{d}z + v^{\mathrm{noise}}_\alpha(\boldsymbol{r}_0, z_0). \quad (3)$$

In terms of the weights, the component of the averaging kernel $\mathcal{K}^\alpha_\beta$ is expressed by

$$\mathcal{K}^\alpha_\beta(\boldsymbol{r}, z; z_0) = \sum_a \int_\odot w^\alpha_a(\boldsymbol{r}'; z_0) K^a_\beta(\boldsymbol{r} - \boldsymbol{r}', z)\mathrm{d}^2\boldsymbol{r}'. \quad (4)$$

The computation of the inversion weights is a mathematical problem, which usually ends in a need to invert a large ill-posed

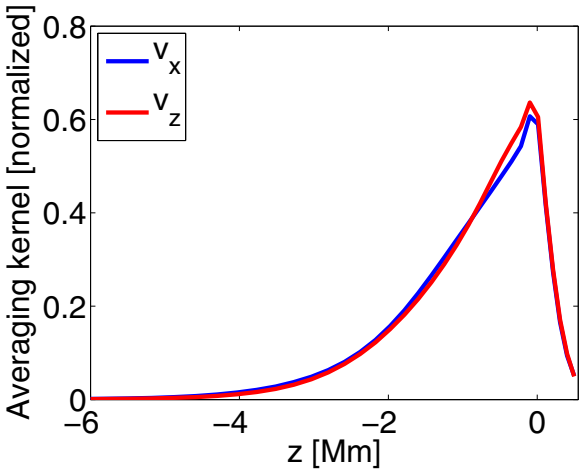

Figure 1. Cuts through the averaging kernel of inversion for horizontal flow (v_x, identical for v_y) and vertical flow (v_z) as a function of depth.
(A color version of this figure is available in the online journal.)

and ill-conditioned matrix. We use the multichannel approach (Jackiewicz et al. 2012) assuming the background is spatially invariant. The multichannel formulation significantly reduces the computational demands.

We used the inversion code that was already validated using synthetic data (Švanda et al. 2011). The inversion we performed was one of the simplest ones. In accordance with the travel-time measurements described above, we utilized sensitivity kernels $\boldsymbol{K}^a$ for the f mode, where a refers to 1 of the 48 possibilities combining 1 of 3 center-to-annulus and center-to-quadrant geometries and 1 of 16 radii of the annuli. The exception was only the inversion for the vertical flow, where we used only the center-to-annulus geometry combined with the 16 distances. The other two geometries, sensitive to waves traveling in the east–west and south–north directions do not contain much information about the vertical flow, do not contribute to the averaging kernels, and just increase the level of noise. We set a requirement on the averaging kernel so that its component in the direction of inversion $\mathcal{K}_\alpha^\alpha$ is strongly localized near the surface (see Figure 1) with a horizontal $\mathrm{FWHM}_h = 10$ Mm and the cross-talk components $\mathcal{K}_\beta^\alpha$ for $\beta \neq \alpha$ are minimized (for details on the process, we refer the reader to Švanda et al. 2011). The bounds on the root-mean-square value of the random-noise component $v_\alpha^{\mathrm{noise}}$ are set to be 25 m s^{-1} and 4 m s^{-1} for the horizontal and vertical components, respectively, when assuming averaging over 12 hr.

2.3. Alignment of Flow Maps from the Two Methods

Unfortunately, although the data entering the two analyses originate from the same telescope and are thus perfectly co-aligned in the beginning, in the course of processing, the coordinate system was changed and the resulting flow maps had to be carefully co-aligned again.

The two-dimensional flow maps from CST were re-projected onto the coordinate grid of the helioseismic datacubes utilizing Postel projection with pixel size of 1.46 Mm, and averaged in time to match the time–distance time span. For each of 4 datacubes, 24 CST flow maps were averaged to form one 12 hr average. Averaging over 12 hr increases the signal-to-noise ratio again. Assuming that the realization noise decreases as $\sqrt{T}$, where T is the length of the time window, the estimate of the noise level in the 12 hr velocities is 50 m s^{-1}.

The exact coordinates of the projection centers and time span are given in Table 1. The angular differential rotation given by

$$\omega(b) = 2.6373 - 0.3441 \sin^2 b - 0.5037 \sin^4 b \, \mu\mathrm{rad/s}, \quad (5)$$

where b stands for the heliographic latitude, was subtracted from the re-projected v_x component. Using this rate, the datacubes for time–distance analysis were tracked, and thus it is natural to remove precisely this rotation profile from the non-tracked CST flow estimate.

3. COMPARISON OF FLOW ESTIMATES

The co-aligned flow maps may be compared directly on a pixel-to-pixel basis. Both methods aim to measure plasma motions on the surface and should ideally match within the noise levels. That actually is almost true. Results coming from both methods have different effective resolutions. The CST flow estimates were computed using the full-resolution HMI intensitygrams and then binned seven times, thus the effective resolution is 3.″5. The flow estimates from the time–distance inversion are obtained with the averaging kernel with $\mathrm{FWHM}_h = 10$ Mm, thus having an effective resolution of 13.″7, which is much coarser. Hence, the flow maps from the CST pipeline must naturally contain flows on smaller scales, which is clearly seen, e.g., in Figure 2 when comparing the left and right columns. To make flow maps from both methods comparable, we convolved the velocity field from the CST code with a cut through the averaging kernel $\mathcal{K}_\alpha^\alpha$ taken at $z = 0$. The smoothed components of the CST flow are also displayed in Figure 2 in the middle column.

Pixel-to-pixel statistics for all four datacubes are summarized in Table 2. It gives the correlation coefficient CC for both horizontal components (for the curious reader, the correlation coefficient with non-smoothed flow estimate from CST is given in parentheses).

The comparison by eye from Figure 2 reveals similarities but also some differences. To make the comparison more straightforward, we also plot values coming from both methods against each other in Figure 3. The slope of the best least-squares fit through the data points using random errors in both variables (York et al. 2004) is also given in Table 2. The values measured by seismology are systematically smaller (by 3%–5%) than those measured by granule tracking. Such discrepancy can easily be explained by additional averaging of helioseismic flow estimates in the vertical direction. When assuming that the flow magnitude peaks just at the surface and its magnitude drops rapidly in larger heights and also decreases with depth, the smoothing with the averaging kernels naturally leads to lower amplitudes. Possible large-magnitude (almost 1 km s^{-1}) horizontal flows at depths around 1.6 Mm suggested by Duvall & Hanasoge (2012) do not affect this conclusion, because, as pointed out by Švanda (2012), in inversion regularized strongly about the noise term, which is also the case here, the possible large-amplitude flows are largely smeared by the extended side-lobes of the averaging kernel. The spread of points seen in Figure 3 seems to be very consistent with the levels of random errors estimated for both methods.

An additional source of differences originates from the fact that both methods may not sample (or sample differently) the horizontal velocities of the same layers: granules move because their convective flux moves so the sampling function (vertical extent of the averaging kernel) of granules is the shape of their convective flux (see Rieutord et al. 2001). On the other hand,

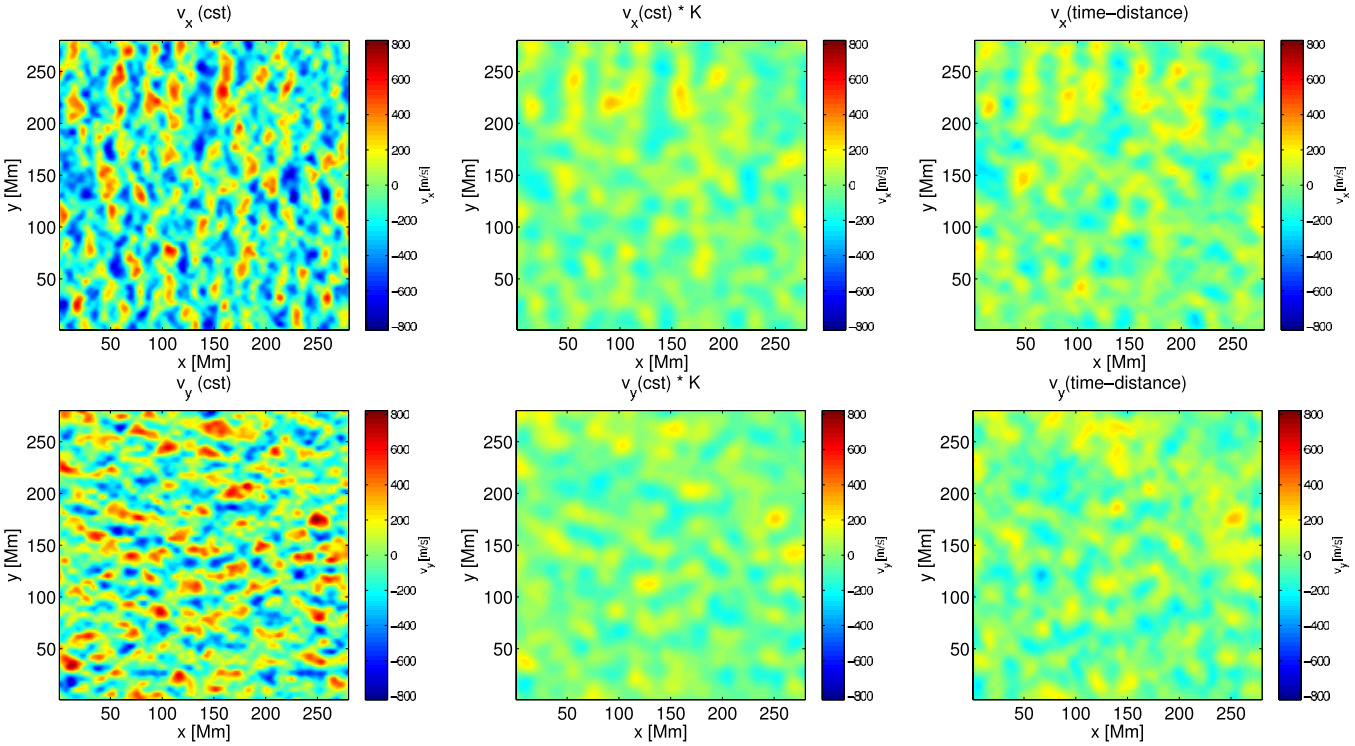

Figure 2. Example maps of horizontal flow velocities (v_x upper row and v_y bottom row) measured from datacube No. 3. Displayed are (from left) the CST-tracked velocity, granule motion velocity convolved with the inversion averaging kernel, and estimate of the flow component from the inversion.

(A color version of this figure is available in the online journal.)

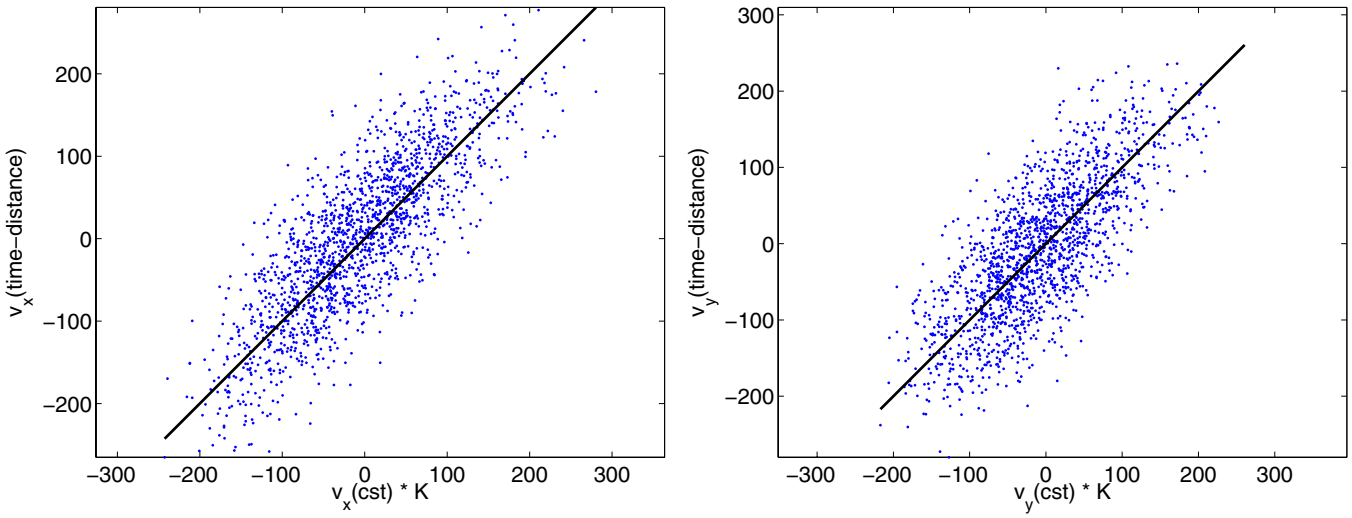

Figure 3. Direct comparison of values of flow estimates from the two methods for independent points in the field of view. The line with the slope of unity represents the location where all points should lie in case both flow estimates are identical.

(A color version of this figure is available in the online journal.)

Table 2
Statistical Values for Comparison of Results of the Two Methods

Cube No.	CC($v_{x,\mathrm{cst}}$, $v_{x,\mathrm{td}}$)	CC($v_{y,\mathrm{cst}}$, $v_{y,\mathrm{td}}$)	Slope($v_{x,\mathrm{cst}}$, $v_{x,\mathrm{td}}$)	Slope($v_{y,\mathrm{cst}}$, $v_{y,\mathrm{td}}$)
1	0.78 (0.60)	0.75 (0.57)	0.97	0.94
2	0.78 (0.59)	0.73 (0.56)	0.94	0.89
3	0.82 (0.63)	0.76 (0.56)	0.96	0.93
4	0.79 (0.61)	0.73 (0.56)	0.95	0.85

Note. We give the correlation coefficient CC of the horizontal flow components and the slope of the least-squares fit to the flow estimates obtained by the two methods.

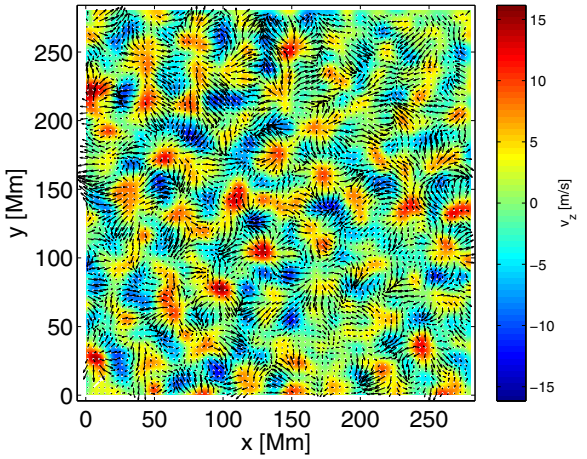

Figure 4. Example of a full-vector flow map; the horizontal components are denoted by arrows (reference arrow indicates flow 250 m s^{-1}), and the vertical component is denoted by colors.

(A color version of this figure is available in the online journal.)

the *f*-mode has another vertical profile which leads to another vertical sampling of the horizontal flow.

The location of the points, where the difference of the flow components measured by the two methods is significant (i.e., the speed values are above their respective noise levels for both methods and the difference is higher than the threshold to be discussed further), is random in the field of view—these points do not correlate with the respective flow estimates. The threshold was determined from a simple model of the expected variance of the difference of two random variables, i.e., $\sigma_{\rm difference} = \sqrt{\sigma_{\rm cst}^2 + \sigma_{\rm td}^2}$. The value of the theoretical threshold (55 m s^{-1}) is close to the variance of 62 m s^{-1} determined from studying the histogram of the differences of flow estimates from the two methods. The use of the latter value does not change the previous statement.

The comparison presented here serves as indication that the helioseismic pipelines provide reasonable estimates of flows. It turns out that by directly comparing the velocity fields coming from granule tracking on the surface, we do not see any significant systematic errors.

4. VERTICAL FLOW

Helioseismic inversion allows us to measure the relatively weak vertical flow at the surface (due to the possibility of minimizing the cross-talk; Švanda et al. 2011). The vertical velocity is usually not evaluated from helioseismic inversion and is usually modeled from the horizontal components assuming mass conservation. In our case all three flow components are inverted independently (an example of the full flow map denoting horizontal components with arrows and vertical components with color is displayed in Figure 4).

To test qualitatively the sensibility of the vertical flow inversion, we utilize the comparison of the vertical flow with the divergence of the horizontal flow, both measured by time–distance helioseismology. The averaging kernels are almost identical (see Figure 1), and thus the flow components are inverted consistently. One would expect (due to the expected mass conservation of plasma flows and negligible horizontal variations in density) that divergent regions in the horizontal flow correspond to upflows in the vertical flow. Such behavior is visible in Figure 4. Quantitatively, the correspondence can be evaluated by means of a correlation coefficient between v_z and $\partial_x v_x + \partial_y v_y$, which is summarized in Table 3. The correlation is positive and significant. The correlation coefficient is expected to be higher; however, one has to bear in mind that the horizontal and vertical flow components have different signal-to-noise ratios. That is estimated to be RMS$(v_\alpha)/\sigma_\alpha$ and has values of 4.0 for the horizontal and 1.1 for the vertical components. Consequently, the signal-to-noise ratio of the horizontal divergence has the value of 1.6. Thus, one cannot expect perfect correspondence.

Table 3
Correlation between Vertical Flow v_z and the Horizontal Divergence of the Horizontal Flow and Correlation between the Measured Doppler Velocity and the Vector Velocity Field Projected into the Line of Sight

Cube No.	CC(v_z, $\partial_x v_x + \partial_y v_y$)	CC($v_{\rm f}$, $v_{\rm los}$)
1	0.50	0.59
2	0.47	0.57
3	0.49	0.64
4	0.52	0.51

4.1. Comparison with Surface Dopplergram

An additional surface measurement of the plasma flow exists, which can also be used to independently verify the results of the time–distance inversion for flows. It is the direct measurement of the Doppler component of velocity $v_{\rm d}$, the high-cadence series of which is used to measure the travel times. Such comparison was already done in the past, e.g., by Gizon et al. (2000). In order to compare with the Doppler component, one has to project the velocity vector in the Cartesian system (v_x, v_y, v_z) to the line-of-sight component $v_{\rm los}$ and two complementary transversal components (v_ξ, v_ζ) using the heliographic coordinates of each point of the flow map, which are known from the definition of the Postel projection. The transformation equations are given in matrix form for illustration:

$$\begin{bmatrix} v_\xi(\boldsymbol{r}) \\ v_\zeta(\boldsymbol{r}) \\ v_{\rm los}(\boldsymbol{r}) \end{bmatrix} = \begin{bmatrix} 1 & 0 & 0 \\ 0 & \cos\varphi(\boldsymbol{r}) & -\sin\varphi(\boldsymbol{r}) \\ 0 & \sin\varphi(\boldsymbol{r}) & \cos\varphi(\boldsymbol{r}) \end{bmatrix} \times \begin{bmatrix} \cos\vartheta(\boldsymbol{r}) & 0 & -\sin\vartheta(\boldsymbol{r}) \\ 0 & 1 & 0 \\ \sin\vartheta(\boldsymbol{r}) & 0 & \cos\vartheta(\boldsymbol{r}) \end{bmatrix} \begin{bmatrix} v_x(\boldsymbol{r}) \\ v_y(\boldsymbol{r}) \\ v_z(\boldsymbol{r}) \end{bmatrix}, \quad (6)$$

where $\vartheta(\boldsymbol{r}) = l(\boldsymbol{r}) - l_0$ and $\varphi(\boldsymbol{r}) = b(\boldsymbol{r}) - b_0$ are the heliocentric coordinates, computed from the Carrington coordinates l and b.

The reference Dopplergram for each of the four datacubes was derived as a temporal average of all high-cadence Dopplergrams over 12 hr. As in the case of the comparison to the horizontal flow derived from granule tracking discussed in Section 3, the direct Dopplergram is obtained with a different effective spatial resolution. Thus, it must contain information on scales smaller than the results from the flow inversion, which acts as noise and naturally decreases the correlation with the projected line-of-sight velocity. Thus, as in Section 3, we convolved the averaged Dopplergram with the horizontal section of the inversion averaging kernel. An example of three comparable maps (Dopplergram, spatially averaged Dopplergram, and a line-of-sight velocity projection) is displayed in Figure 5. The Pearson correlation coefficient between the latter two for each of the four datacubes investigated is given in Table 3. The correlation is positive and significant. Note that Gizon et al. (2000) mention a slightly higher correlation between the Dopplergram and line-of-sight projection (correlation coefficient of 0.7). The

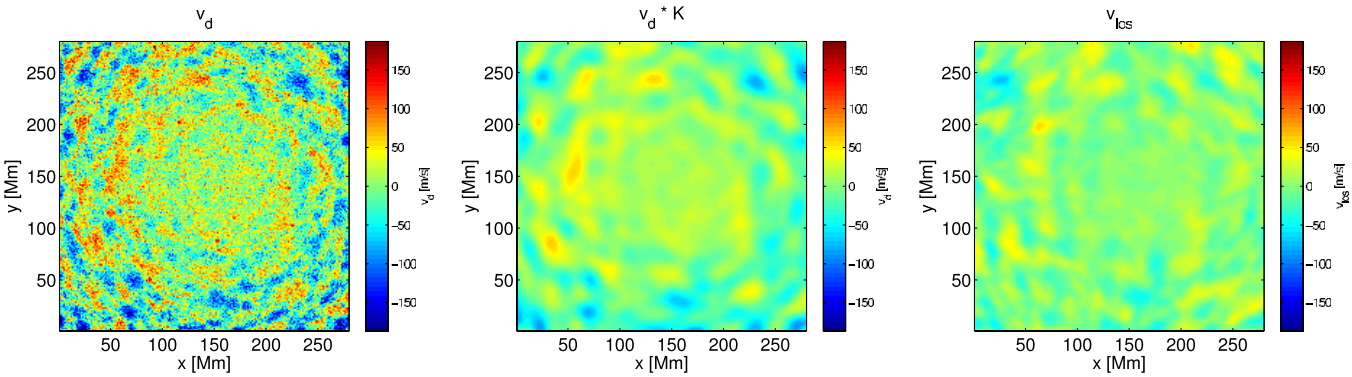

Figure 5. Comparison of the measured Doppler component of the velocity (left), the measured Dopplergram convolved with the averaging kernel (middle), and the time–distance vector flow estimate projected onto the line of sight (right). One sees a striking correspondence between the middle and right panels.

(A color version of this figure is available in the online journal.)

lower correlation coefficient in our study originates from the region at the disk center, where the weak (and quite noisy) vertical component v_z of the flow dominates the projected line-of-sight velocity. When the v_z is excluded (set to zero) from the line-of-sight velocity projection, the correlation coefficient is higher by 0.05 for all four datacubes. When the center-of-the-disk region is omitted (central 70 Mm), the correlation coefficient increases by an additional 0.03.

4.2. Density Scale Height

From a direct comparison between the horizontal and vertical components of the flow, we estimated the density scale height. Let us start by separating the density ρ and velocity vector $\mathbf{v}$ into the time-averaged components $\overline{\rho}$ and $\overline{\mathbf{v}}$ and fluctuations ρ' and $\mathbf{v}'$. Thus, the continuity equation now reads

$$\frac{\partial \rho'}{\partial t} + \nabla \cdot \{(\overline{\rho} + \rho')(\overline{\mathbf{v}} + \mathbf{v}')\} = \mathbf{0}. \quad (7)$$

By taking the time average of Equation (7) and assuming that $\overline{\rho'} = 0$ and $\overline{\mathbf{v}'} = 0$, we obtain

$$\overline{\mathbf{v}} \cdot \nabla \ln \overline{\rho} + \nabla \cdot \overline{\mathbf{v}}_h + \frac{\partial \overline{v}_z}{\partial z} + \frac{1}{\overline{\rho}} \nabla \cdot \overline{\rho' \mathbf{v}'} = 0 \quad (8)$$

where $\overline{\mathbf{v}}_h$ is the average horizontal velocity. Finally we obtain

$$\overline{v}_z \frac{\partial \ln \overline{\rho}}{\partial z} + \nabla \cdot \overline{\mathbf{v}}_h = -\frac{\partial \overline{v}_z}{\partial z} - \frac{1}{\overline{\rho}} \nabla \cdot \overline{\rho' \mathbf{v}'} \quad (9)$$

where we assumed that the averaged density depends only on depth. We see that if the right-hand side is negligible, then the horizontal divergence and the vertical velocity are correlated. Moreover, the slope of the correlation gives the scale height of the density $H_\rho = -[\partial \ln \overline{\rho} / \partial z]^{-1}$. Since the horizontal and vertical velocities are from the same layers, the correlation slope gives a weighted average of the density scale height at the sampled depth.

Doing the exercise, the least-squares fit of the data by a linear law using the known error levels in both variables (York et al. 2004) gives an estimate for the density scale height in the near-surface layers, which we find to be around 180 km. Such a value is on the same order as the 125 km found by November (1994) from a study of supergranulation. By simply taking the density scale height from Model S (Christensen-Dalsgaard et al. 1996) and integrating it over the inversion averaging kernel, we get a value of 535 km, which is three times larger than the scale height determined from the inversion. However, one should note that the density scale height determination is a sanity check of inversion consistency. Additionally, due to the presence of additional terms in Equation (9), one cannot expect a better than an order of magnitude agreement with the stationary solar model.

5. CONCLUSION

We measured surface horizontal flows using both CST and three-dimensional time–distance inversions. The measurements from the two techniques are in good agreement. Our future goals will focus on studies of plasma dynamics, especially on studies of solar convection (see Gizon & Birch 2012; Hanasoge et al. 2012).

M.Š. is supported by the Czech Science Foundation (grant P209/12/P568). This study was supported by the European Research Council under the European Community's Seventh Framework Programme (FP7/2007–2013)/ERC grant agreement #210949, "Seismic Imaging of the Solar Interior," to PI L. Gizon (Milestone #5). L.G. acknowledges research funding by Deutsche Forschungsgemeinschaft (DFG) under grant SFB 963/1 "Astrophysical Flow Instabilities and Turbulence" (Project A1). This work utilized the resources and helioseismic products provided by the German Data Center for the Solar Dynamics Observatory (GDC-SDO), which is hosted by the MPS in Katlenburg-Lindau, Germany, and funded by the German Aerospace Center (DLR). The data were kindly provided by the HMI consortium. The HMI project is supported by NASA contract NAS5-02139. Tato práce vznikla s podporou na dlouhodobý koncepční rozvoj výzkumné organizace RVO:67985815 a výzkumného záměru MSM0021620860.

REFERENCES

Ambrož, P. 2005, in ASP Conf. Ser. 346, Large-scale Structures and their Role in Solar Activity, ed. K. Sankarasubramanian, M. Penn, & A. Pevtsov (San Francisco, CA: ASP), 3
Birch, A. C., & Gizon, L. 2007, AN, 328, 228
Christensen-Dalsgaard, J., Dappen, W., Ajukov, S. V., et al. 1996, Sci, 272, 1286
De Rosa, M., Duvall, T. L., Jr., & Toomre, J. 2000, SoPh, 192, 351
Dombroski, D. E., Birch, A. C., Braun, D. C., & Hanasoge, S. M. 2013, SoPh, 282, 361
Duvall, T. L., & Hanasoge, S. M. 2012, SoPh
Duvall, T. L., Jr., Jefferies, S. M., Harvey, J. W., & Pomerantz, M. A. 1993, Natur, 362, 430

Duvall, T. L., Jr., Kosovichev, A. G., Scherrer, P. H., et al. 1997, SoPh, 170, 63
Georgobiani, D., Zhao, J., Kosovichev, A. G., et al. 2007, ApJ, 657, 1157
Gizon, L., & Birch, A. C. 2004, ApJ, 614, 472
Gizon, L., & Birch, A. C. 2012, PNAS, 109, 11896
Gizon, L., Birch, A. C., & Spruit, H. C. 2010, ARA&A, 48, 289
Gizon, L., Duvall, T. L., Jr., & Larsen, R. M. 2000, JApA, 21, 339
Hanasoge, S. M., Duvall, T. L. J., & Sreenivasan, K. R. 2012, PNAS, 109, 11928
Hindman, B. W., Gizon, L., Duvall, T. L., Jr., Haber, D. A., & Toomre, J. 2004, ApJ, 613, 1253
Jackiewicz, J., Birch, A. C., Gizon, L., et al. 2012, SoPh, 276, 19
Jackiewicz, J., Gizon, L., & Birch, A. C. 2008, SoPh, 251, 381
Mallat, S. G. 1989, ITPAM, 11, 674
November, L. J. 1986, ApOpt, 25, 392
November, L. J. 1994, SoPh, 154, 1
Pijpers, F. P., & Thompson, M. J. 1992, A&A, 262, L33
Rieutord, M., Meunier, N., Roudier, T., et al. 2008, A&A, 479, L17
Rieutord, M., Roudier, T., Ludwig, H.-G., Nordlund, Å., & Stein, R. 2001, A&A, 377, L14
Rieutord, M., Roudier, T., Rincon, F., et al. 2010, A&A, 512, A4
Rieutord, M., Roudier, T., Roques, S., & Ducottet, C. 2007, A&A, 471, 687
Roudier, T., Rieutord, M., Malherbe, J. M., et al. 2012, A&A, 540, A88
Roudier, T., Rieutord, M., Prat, V., et al. 2013, A&A, 552, A113
Scherrer, P. H., Schou, J., Bush, R. I., et al. 2012, SoPh, 275, 207
Schou, J., Scherrer, P. H., Bush, R. I., et al. 2012, SoPh, 275, 229
Švanda, M. 2012, ApJ, 759, L29
Švanda, M., Gizon, L., Hanasoge, S. M., & Ustyugov, S. D. 2011, A&A, 530, A148
Švanda, M., Klvaňa, M., & Sobotka, M. 2006, A&A, 458, 301
Švanda, M., Zhao, J., & Kosovichev, A. G. 2007, SoPh, 241, 27
Tkaczuk, R., Rieutord, M., Meunier, N., & Roudier, T. 2007, A&A, 471, 695
York, D., Evensen, N. M., Martinez, M. L., & Delgado, J. D. 2004, AmJPh, 72, 367
Zhao, J., Georgobiani, D., Kosovichev, A. G., et al. 2007, ApJ, 659, 848